Ligand-Free MAPbI₃ Quantum Dot Solar Cells Based on Nanostructured Insulating Matrices

Andrea Rubino, Laura Caliò, Mauricio E. Calvo,* and Hernán Míguez*

The stability, either chemical or thermal, and performance of colloidal quantum dot (CQD) devices are typically limited by the presence of surface-bonded organic ligands required to stabilize the nanocrystals. In addition, optimization of charge transport implies lengthy ligand exchange processing. Herein, evidence of efficient charge transport through a network of ligand-free perovskite quantum dots (PQDs) embedded in an insulating porous matrix made of monodisperse SiO_2 nanoparticles is shown. Methylammonium lead iodide ($CH_3NH_3PbI_3$ or $MAPbI_3$) QDs are prepared in situ by infiltration of precursors within the matrix pores, which act both as nanoreactors for the synthetic reaction and as supporting scaffolds, hence reducing the number of synthetic and postprocessing steps usually required in CQD solar cells. Above a certain nanocrystal load, charge percolation is reached and dot-to-dot transport achieved without compromising quantum confinement effects. Solar cells based on MAPbI₃ QDs prepared in this way present a 9.3% efficiency, the highest reported for a scaffold-supported PQD solar cell, and significantly improved stability under solar illumination with respect to their bulk counterparts. Therefore, adequately designed networks of ligand-free PQDs can be used as both light harvesters and photocarrier conductors, in an alternative configuration to that used in previously developed QD solar cells.

1. Introduction

Barely a decade after the first perovskite-based solar device was presented by Miyasaka and co-workers,[1,2] perovskite solar cells (PSCs), which have reached power conversion efficiency (PCE) values above 25%,[3] are already rivalling other more established semiconductor photovoltaic technologies. Nevertheless, despite the progress achieved in the last few years, some issues remain unsolved, such as hysteresis[4] and, more importantly, instability derived from moisture/thermal sensitivity and photoinduced ion migration,[5] which constitute impediments toward device commercialization.[6] A promising approach to overcome these issues is based on the synthesis of low-dimensional perovskites, among which perovskite quantum dots (PQDs) are catalogued.[7,8] Nanoscale perovskite materials present substantial advantages over large-grain perovskite thin films or *bulk*,[9] such as high photoluminescence quantum yield (PLQY),[10] photon up- and down-conversion,[11] multiexciton generation,[12] enhanced defect tolerance,[13,14] and improved stability.[15] Furthermore, bandgap tuning by quantum confinement effects, achieved by controlling the nanocrystal dimensions, make them particularly suitable for applications in tandem solar cells,[16] which are solid candidates to reach PCE values that surpass the Shockley–Queisser limit.

There are currently two main configurations in which PQDs are implemented in a photovoltaic device. In one of them, proposed originally by Park and co-workers in 2011,[17] PQDs are used as sensitizers capable of harvesting light and injecting photogenerated charges directly into the conduction band of a metal-oxide-based scaffold. This approach has been further developed since then and has given rise to devices with PCEs as large as 7.2%.[18–20] In this same direction, a few subsequent works explored the use of insulating matrices, such as aluminum oxide,[21] zirconium oxide,[22] silicon oxide,[23] and a combination of those.[24] However, in none of those works clear evidence of strict control over the perovskite nanocrystal dimensions is provided,[18,20,22,23] nor, most importantly, quantum confinement effects explicitly demonstrated in the optoelectronic behavior of the devices,[17,20–26] therefore not fulfilling the requirements to be considered PQD devices. From another perspective, after relevant advances realized in the preparation of colloidal PQDs (CPQDs) by hot injection,[27] Luther and co-workers developed the first scaffold-free CPQD solar cell.[28] Further progresses based on this approach have improved CPQD solar cells to the point that they currently hold, with a 16.6% PCE, the record among all semiconductor QD solar cells.[29]

Despite all these achievements, further development of CPQD solar cells faces relevant challenges.[30–33] One of them regards the presence of insulating organic molecules around the as-synthesized PQDs, which are used as protective ligands to prevent aggregation. These ligands limit the chemical and thermal stability of the devices made with them and, most

Dr. A. Rubino, Dr. L. Caliò, Dr. M. E. Calvo, Prof. H. Míguez
Instituto de Ciencia de Materiales de Sevilla
Consejo Superior de Investigaciones Científicas-Universidad de Sevilla
C/Américo Vespucio 49, 41092 Sevilla, Spain
E-mail: mauricio.calvo@csic.es; h.miguez@csic.es

importantly, hinder charge transport, which, to be optimized, requires lengthy purification and ligand exchange processing.[34] This will necessarily increase the cost of CPQD devices, which might compromise their commercialization. Also, in terms of available compositions, which provide a means to realize bandgap and hence voltage engineering in the CPQD solar cell, candidates are limited to those colloids that can stand the processing required to integrate them in a solar cell. This limits the available compositions to $CsPbX_3$ (X = Br, I), $FAPbI_3$ (FA, formamidinium, $CH(NH_2)_2$) or double organic–inorganic cation ones such as $Cs_xFA_{(1-x)}PbI_3$ QDs.[35] It is precisely the lack of stability of colloidal $MAPbI_3$ QDs that has prevented the preparation of a solar cell based on this paradigmatic compound.

Herein, we present stable, ligand-free, $MAPbI_3$ QD solar cells with power conversion efficiencies above 9%. $MAPbI_3$ QDs are synthesised in situ within a porous silica (SiO_2) matrix with a narrow nanopore size distribution. This translates into a fine control over the QD size and thus over the spectral position of their electronic bandgap, preventing energetic disorder that could affect the performance of the devices built with them. Above a certain QD load level within the matrix, dot-to-dot charge transport occurs, although well-defined quantum confinement effects are still observed. The structure of the matrix, apart from playing a key role in the synthesis, provides a protective and stabilizing environment for the embedded nanocrystals, as revealed by the significantly improved stability under constant solar illumination with respect to bulk or colloidal $MAPbI_3$. These devices operate within the strong quantum confinement regime, as evidenced by their spectral features (i.e., blueshift of the light-harvesting efficiency and of photoluminescence), in good agreement with the analysis of high-resolution transmission electron microscopy (HRTEM) images. Insight on the transport mechanism is attained by impedance spectroscopy, which is used to provide a detailed description of the different regimes of charge percolation as a function of PQD load.

2. Results and Discussion

2.1. Solar Cells Based on Ligand-Free PQDs

$MAPbI_3$ QDs are synthesized by impregnating a perovskite precursor solution in insulating porous thin films of 400 nm thickness made of nearly monodisperse packed SiO_2 nanoparticles (30 nm), following a procedure thoroughly described elsewhere,[36,37] which ensures that the narrow pore size distribution of the matrix is inherited by the nanocrystals grown within. The pores act as interconnected nanoreactors that yield nanocrystals of well-defined size and display controllable quantum confinement effects. This approach can make use of a variety of mesostructured materials,[38,39] mostly metal oxides, with a wide range of pore sizes and geometries, and permits us to synthesize PQDs of very diverse composition.[40] In Figure S1 and S2, Supporting Information, we show scanning electron microscopy (SEM) images of the SiO_2 scaffold used herein, as well as the results of the analysis of its pore size distribution and the X-ray diffractograms of the PQDs synthesized within.

The ability of these perovskite-nanocrystal-impregnated films to transport and inject photogenerated charges was tested by integrating them in canonical perovskite solar cell architectures. Onto

a transparent conducting fluorinated tin oxide (FTO), an electron-transporting layer (ETL) made of dense TiO_2 (d-TiO_2), a $MAPbI_3$-QD-impregnated nanoporous SiO_2 film, a hole-transporting layer (HTL) of 2,2′,7,7′-Tetrakis[N,N-di(4-methoxyphenyl)amino]-9,9′-spirobifluorene (Spiro-OMeTAD), and a metallic gold contact were sequentially deposited. **Figure 1**a shows a schematic representation of the configuration used, while in Figure 1b a cross-sectional SEM image shows the different layers constituting the device. In Figure 1c, the results of energy dispersive X-ray (EDX) chemical mapping of a cross-section, and its corresponding high-angle annular dark-field scanning TEM (HAADF-STEM) image, are shown. Perovskite nanocrystals are homogeneously distributed along the scaffold, as can be seen from the maps of iodine (red) and lead (blue) atoms. Also, it shows that Spiro-OMeTAD is directly in contact with $MAPbI_3$ nanocrystals because it infiltrates the upper portion of the nanoporous scaffold. This is relevant to ensure the electrical contact between all charge-transporting layers in the device. A closer look at the cross-section of a PQD@SiO_2 film confirms that the PQDs are homogeneously dispersed in the scaffold, as shown in Figure 1d,e, where images taken by HRTEM from a lamella obtained by a focused ion beam (FIB) are shown.

To ensure that device-integrated nanocrystals are actually QDs (i.e., show quantum confinement effects), photoluminescence (PL) spectra from devices prepared using increasing precursor concentrations in the infiltrated solution were measured.

Results are plotted in Figure 1d (red, blue, and purple solid lines). The PL of a bulk $MAPbI_3$ film is also plotted for the sake of comparison (gray dashed line). The PL blueshifts observed (28, 53, and 56 meV) are unequivocal signs of the confinement of the exciton wave functions inside the $MAPbI_3$ crystals and prove their QD character. Considering the exciton Bohr radius of bulk $MAPbI_3$ of 3 nm,[41] we can estimate the PQD size based on the Brus formula,[42] in each case a PQD radius of 2.5, 4, and 5 nm being attained. The absorptance spectra of the active layers confirm a similar blueshift of the optical band edge as the radius of the PQD decreases (Figure S3, Supporting Information). The PQD load in each device was estimated using inductively coupled plasma (ICP) atomic emission spectrometry, which yielded total volume filling fractions of 45%, 41%, and 26%, respectively (90%, 82%, and 52% of the pore volume, as silica particles occupy 50% of the film volume).

The PQD devices so prepared exhibit a photoelectric behavior characteristic of a solar cell. In **Figure 2**a,b, the electrical current density versus voltage (J–V) attained under 1 sun illumination (AM 1.5) and the incident photon to current efficiency (IPCE) curves recorded for the best performing devices attained for each crystal size are plotted. Reverse and forward bias illuminated scans, as well as integrated photocurrent densities, are shown in Figure S4a,b, Supporting Information, respectively. Data obtained from both graphs are shown in Table S1 and S2, Supporting Information.

It should be noted that devices with a low concentration of PQDs (<10% of the pore volume) did not show photovoltaic conversion, likely due to the poor charge transport resulting from a too dispersed distribution of the QDs. Above that threshold, the photocurrent increases with the load of PQDs in the porous film. We find an excellent agreement between the short circuit photocurrent density J_{SC} obtained from the J–V curves and the integrated photocurrent density extracted from the IPCE
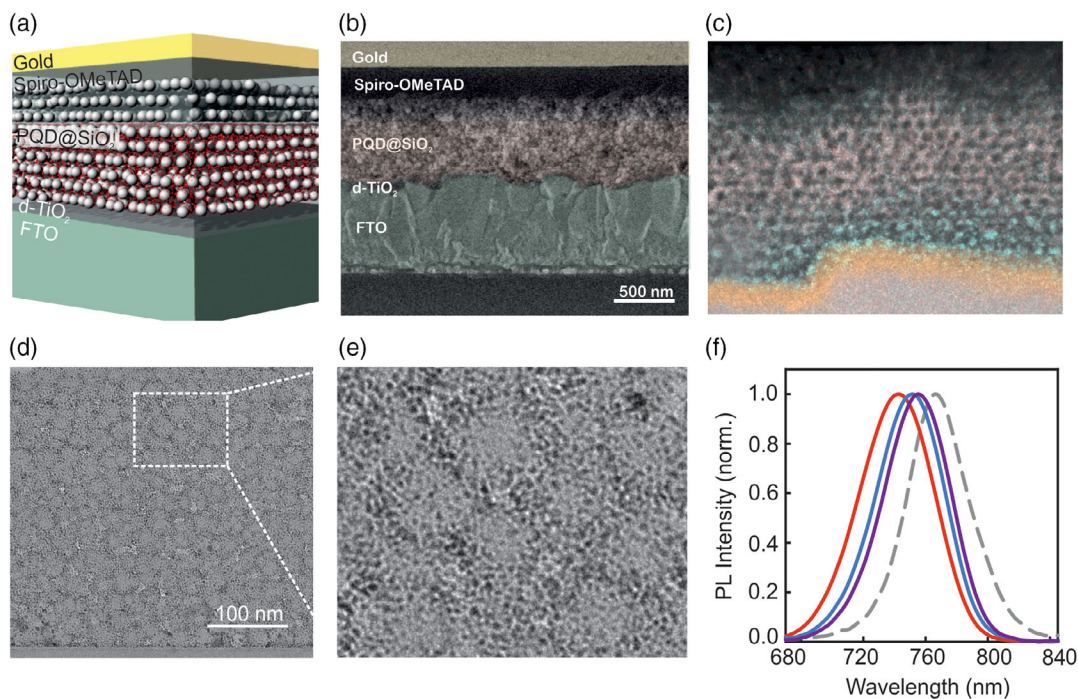
Figure 1. a) Scheme of designed PQD solar cell. b) Secondary electron SEM image of a cross-section of a representative $MAPbI_3$ QD solar cell based on a 400 nm thick nanoporous SiO_2 matrix. Colors highlight the different layers constituting the device. c) EDX chemical mapping of a TEM (HAADF-STEM) image of a cross-section of a $MAPbI_3$ QD solar cell in which different element maps are shown in different colors: Sn (gray), Ti (orange), Pb (light blue), and I (red). d,e) HRTEM images at different magnifications of a PQD@SiO_2 layer. f) Photoluminescence spectra recorded from three SiO_2 films embedding $MAPbI_3$ QDs of different estimated average diameters, namely, 5 nm (red solid line), 8 nm (blue solid line), and 10 nm (purple solid line). The PL from a bulk film $MAPbI_3$ (gray dashed line) is included for the sake of comparison.

measurements. The best performing device gives a PCE of 9.3%, which corresponds to the largest concentration of nanocrystals achieved (45%, average nanocrystal diameter of 10 nm), attained using a concentration of reactants in the precursor solution close to saturation. In Figure 2c, we show the statistical analysis of the main photovoltaic parameters (i.e., open circuit voltage, V_{OC}, J_{SC}, fill factor, FF, and PCE) recorded for different cells. In all cases, the values attained from a standard planar $MAPbI_3$ film based solar cell are also plotted for the sake of comparison (dashed gray lines in Figure 2a,b, gray boxes in Figure 2c–f). Please note that, because the scaffold is an insulator, the electric current through the device can only take place if photocarriers percolate through the porous network as a result of its transport between adjacent QDs. As summarized in **Table 1**, the different devices present a high V_{OC} and comparable values of FF, the main differences being found in the current densities attained, which are directly related to the concentration of perovskite QDs, and hence to their ability of harvesting light and transport carriers. Similar trends were found when perovskite nanocrystals were synthetized in a 12 nm diameter SiO_2 nanoparticle scaffold (as shown in Figure S5, Supporting Information). Even if with slightly poorer photovoltaic performance, which may be attributed to the lower density of nanocrystals within the scaffold, all devices showed a significant photocurrent.

One key issue in the field of perovskite solar cells is that of instability, which arises from a combination of factors such as ion migration, photoinduced changes of the chemical structure,

and, in general, the extreme sensitivity of metal halide perovskites to their surroundings.[43] To test the stability of the PQD devices herein reported, we studied the evolution of their main photovoltaic parameters under illumination for 5 h. Similar measurements were conducted for standard cells based on bulk films for the sake of comparison. Results are shown in **Figure 3**, where all values have been normalized by dividing by the one initially measured (time $t = 0$). It can be readily seen that solar cells based on PQDs embedded in the porous scaffold present a more stable performance than their bulk counterpart. This indicates that the insulating nanoporous host provides not only control over the size and dispersion of the QDs, but also a protective environment for the perovskite. Also, ion migration, a deleterious phenomenon in terms of its effect over device performance, is likely to be highly reduced as a consequence of the lower density of defects in the QDs. Detailed plots showing the stability analysis of the devices at short times (<5 min) under continuous illumination are also provided in the Supporting Information (see Figure S6, Supporting Information).

2.2. Analysis of Charge Transport in Ligand-Free PQD Solar Cells: Impedance Spectroscopy Analysis

Impedance spectroscopy allows us to discriminate between the different processes occurring at different time scales, such as charge transport or recombination, in a whole and unified picture. The results shown previously are evidence of the capability
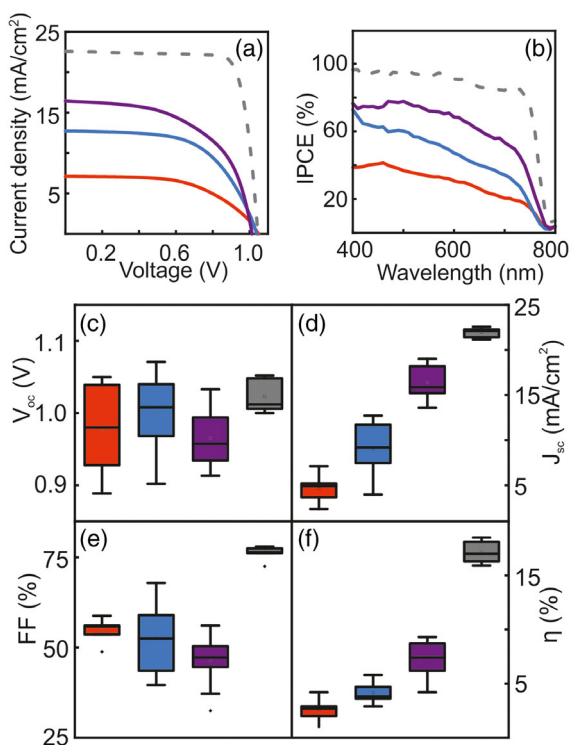
Figure 2. a) J–V and b) IPCE curves of nanostructured perovskite solar cell. c–f) Box plots summarizing the statistic photovoltaic performance of a batch of 28 devices. Purple, blue, and red solid lines and boxes correspond to a 400 nm thick scaffold made of 30 nm diameter SiO_2 nanoparticles, infiltrated with different $MAPbI_3$ precursor solutions, to yield PQD sizes and loads of (10 nm, 45 vol%), (8 nm, 41 vol%), and (5 nm, 26 vol%), respectively. The gray dashed lines and boxes correspond to a reference cell made of bulk $MAPbI_3$ in planar configuration.

Table 1. Summary of the photovoltaic parameters recorded for the best devices for each configuration. The devices present the same architecture shown in Figure 2, and diverge just in the PQD size and concentration. "Bulk" refers to a device containing a 300 nm thick $MAPbI_3$ layer in a planar configuration.

$MAPbI_3$	V_{OC} [V]	J_{SC} [mA cm^{-2}]	FF [%]	PCE [%]
(5 nm, 26 vol%)	1.05	7.11	56.1	4.2
(8 nm, 41 vol%)	1.04	12.72	59.0	7.8
(10 nm, 45 vol%)	1.02	16.42	56.1	9.3
Bulk	1.05	22.89	75.3	18.1

of ligand-free perovskite nanocrystal assemblies supported on insulating substrates to support efficient charge separation, transport, and injection into the selective contacts. To gain insight on these conduction properties, we analyzed the devices by impedance spectroscopy (IS). In all cases, we performed IS at 0.1 sun and under bias voltages between V_{OC} and 0 V. We also measured the illuminated voltammograms before and after the IS measurements, to make sure that no degradation occurs during the experiments. In **Figure 4**, we show a series of Nyquist (Z'' vs Z', red lines) and Bode plots (Z versus frequency, scatter
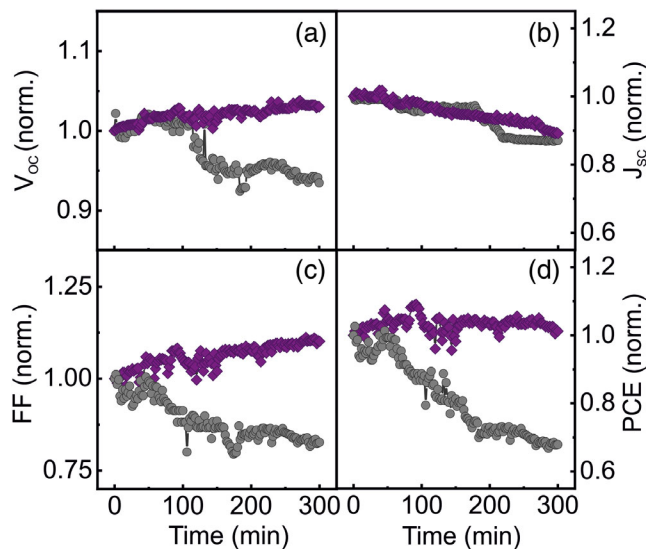

Figure 3. a) V_{OC}, b) J_{sc}, c) FF, and d) PCE data recorded over a period of 5 h for both a $MAPbI_3$ PQD (purple scatters) and bulk planar (gray scatters) devices.

graphs) at V_{OC} attained from the IS analysis of different PSCs. Results for a planar device are shown in Figure 4a,b, while those attained for devices made of PQD@SiO_2 films using different QD sizes and filling fractions are plotted in Figure 4d,e (QD diameter 10 nm, 45 vol%) and Figure 4g,h (8 nm, 41 vol%). Red curves correspond to the best fittings achieved using different equivalent circuits, which are shown in Figure 4c,f,i and described in what follows.

The IS data for a standard planar perovskite solar cell were fitted using the model developed by Bisquert and co-workers, which considers an equivalent circuit such as the one plotted in Figure 4c.[44] In this case, R_s stands for a series resistance, and R_{HF}, R_{LF}, CPE_{HF}, and CPE_{LF} are the resistances and constant phase elements at high and low frequencies, respectively. For the PQD cell characterized by the parameters (10 nm, 45 vol%), best results were attained for the equivalent circuit drawn in Figure 4f, also developed by Bisquert and co-workers.[45] Interestingly, this model introduces a transmission line (TL), which has previously been used to satisfactorily explain the behavior of dye-sensitized solar cells. In them, charges have to percolate through an assembly of TiO_2 nanocrystals used as scaffold.[46] In our case, the insulating scaffold cannot support charge transport; hence, the only network of nanocrystals that can actually conduct electricity is that formed by the PQDs. As we lower the amount of nanocrystals present within the insulating silica matrix, the interconnectivity between crystallites is reduced and transport is gradually hindered. The increase in the hysteresis index as the filling fraction of PDQs reduces also denotes a deterioration in the charge transport or extraction processes. Eventually, recombination resistance becomes smaller than transport resistance and, accordingly, the TL is substituted by a Gerischer resistance (G), in good agreement with previous IS analysis of porous electrodes.[44] Please note that the fittings of the ligand-free nanocrystal cells indicate, as expected, that transport takes place through charge percolation, discarding other conduction channels in the
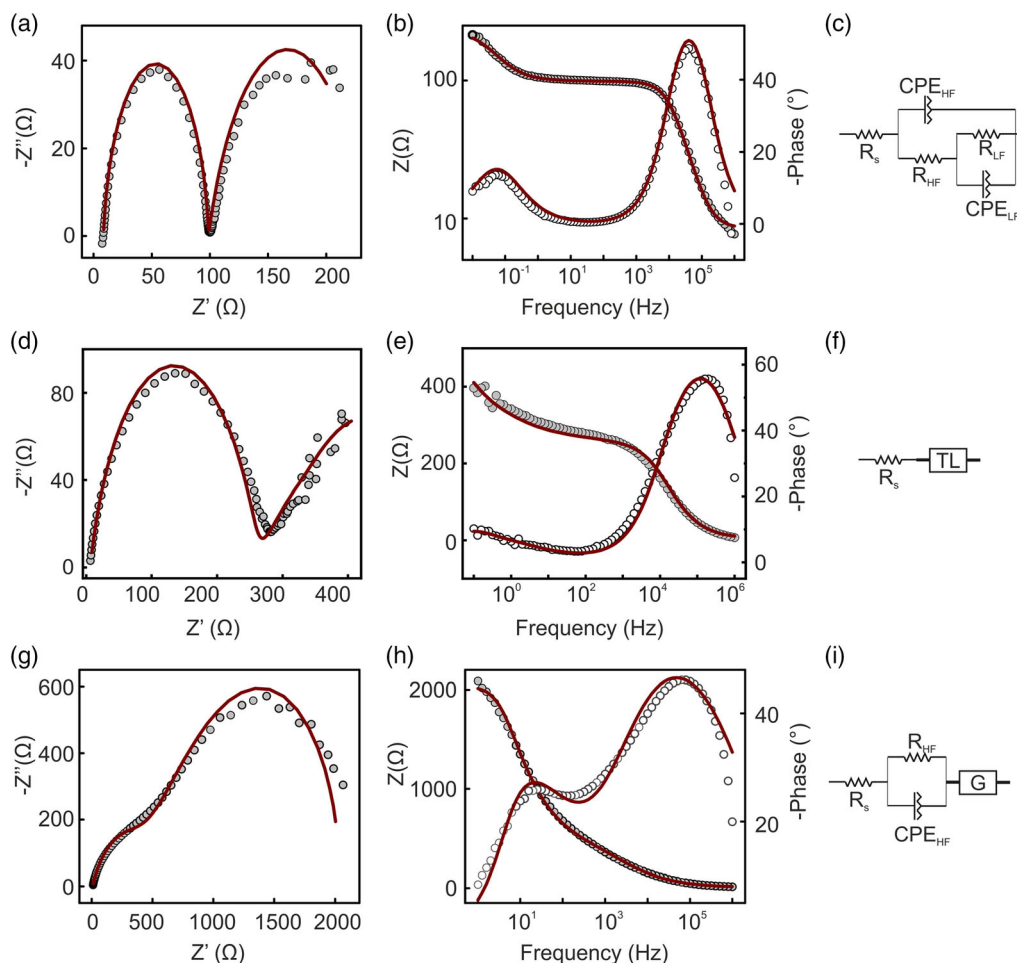
Figure 4. a,d,g) Nyquist and b,e,h) Bode plots measured at $V = V_{OC}$ for a planar thin-film solar cell (a,b), and for two PQD solar cells characterized by nanocrystal sizes and concentrations (10 nm, 45 vol%) (d,e) and (8 nm, 41 vol%) (g,h). In all cases, red solid lines represent the best fit attained using the equivalent circuits described, correspondingly, in (c), (f) and (i).
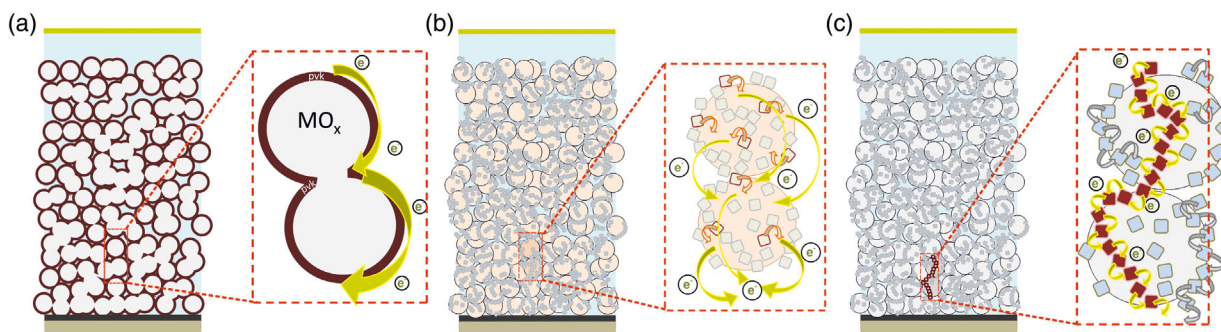

Figure 5. Schemes of the different configurations of scaffold-supported PSCs. a) A thin perovskite layer coats the mesoporous scaffold; charge transport takes place through the interconnected perovskite thin film regardless of the insulating or conducting nature of the scaffold (MO_x). b) A PQD-sensitized solar cell, in which photocarriers are transferred to and conducted by a wide semiconductor bandgap nanocrystalline matrix, typically TiO_2. c) The configuration herein proposed, in which a network of PQDs is supported by an insulating matrix (SiO_2); the charge transport mechanism proposed takes place from dot to dot, based on the results of the IS analysis.

device.[47] For the sake of comparison, in **Figure 5** we schematize both the structure and the charge transport mechanism for the two main configurations of scaffold-supported PSCs, (a) and (b), along with those of the PQD@SiO_2 solar cell herein

proposed, (c), for which we propose a dot-to-dot transport mechanism based on the IS analysis. More details on the specific values of the different electrical parameters, extracted from the different models used, are provided in the Supporting

Information (Table S3, Supporting Information), along with a deeper analysis and physical interpretation of the different elements considered in the equivalent circuits (please see comments under section "Impedance Spectroscopy of PQDs Solar Cell" and Figure S7–S9, Supporting Information).

3. Conclusion

We have shown that it is possible to build ligand-free MAPbI$_3$ PQD solar cells with PCEs exceeding 9% and improved stability with respect to their bulk counterparts. A nanoporous insulating material with a narrow void size distribution is used as the scaffold that acts as a network of nanoreactors, providing control over the synthesis, and therefore over the nanocrystal size attained, and a protective environment that enhances the environmental stability of the device. Impedance spectroscopy analysis of the devices herein presented indicate that, from the point of view of charge transport, the absorbing film behaves as a network of ligand-free PQDs that are capable of efficiently conducting photocarriers while preserving their individual character, as revealed by the fact that they display quantum size effects. In this sense, our proposal implies an alternative approach to those commonly used in QD-based photovoltaics, which rely either on sensitization of a conducting scaffold or on charge transport through an assembly of organic-ligand-coated colloidal nanocrystals. The concept herein presented might ease the production of QD devices as it allows skipping the complex synthetic and postprocessing steps required when organic capping layers are present on the surface of semiconductor nanocrystals.

4. Experimental Section

Nanoporous SiO$_2$ and TiO$_2$ Film Fabrication: A commercial colloidal dispersion of SiO$_2$ (Ludox TMA, d30nm, 34% in water or Ludox CL, d12nm, 30% in water, W.R. Grace) was diluted to 3% (w/v) in methanol. Porous nanoparticle-based films were deposited by dip coating on the substrate treated with O$_2$ plasma to activate the surface. Consecutive immersions of the substrate in the colloidal dispersions were performed, with a withdrawal speed of 100 mm min^{-1}. This method allowed the obtainment of layers with 400 nm, 700 nm and 1 μm thickness, depending on the number of repeated immersions. Then, the films were treated at the temperature of 450 °C to remove the organic compound that stabilized the SiO$_2$ suspension.

TiO$_2$ nanoporous layers were fabricated from a colloidal dispersion of TiO$_2$ nanoparticles of 30 nm diameter, prepared by diluting a commercial TiO$_2$ paste (Dyesol, 30NRD) in EtOH (1:7 w/w). TiO$_2$ was deposited by spin coating (4000 rpm, 30 s) and the samples were annealed by heating up progressively to 450 °C for 1 h.

Solar Cell Fabrication: PSCs were fabricated on FTO-coated glass (TEC 7, Pilkington) patterned by laser etching. Substrates were cleaned using 2% Hellmanex solution, ultrasonicated for 15 min, and rinsed with deionized water. After this, they were sonicated in acetone and 2-propanol, and dried with nitrogen. Oxygen plasma (Diener Femto Plasma cleaner) treatment for 10 min was conducted to eliminate organic impurities and activate the surface. TiO$_2$ compact layer was deposited by spray pyrolysis at 450 °C using 1 mL of titanium diisopropoxide bis(acetyl acetonate) precursor solution (75% in 2-propanol, Sigma-Aldrich) in 19 mL of pure ethanol using dry air as carrier gas, to obtain a 30 nm thick layer. The substrates were kept at 450 °C for an hour and then left to cool down to room temperature. Then, they were treated with TiCl$_4$ (dipping in a 0.02 M TiCl$_4$ solution in deionized water at 70 °C for 30 min) to obtain a homogeneous layer. Next, the samples were washed with deionized water, burned at 500 °C for 30 min, and cooled to room temperature. For the bulk film

based cell, the perovskite layer was deposited by spin coating from a precursor solution prepared by mixing 0.502 g of PbI$_2$ with 0.179 g of methylammonium iodide (MAI) in 1.6 g of a 4:1 (v/v) N,N-dimethylformamide (DMF): dimethyl sulfoxide (DMSO) solution, by a two-step spin-coating program. The solution was first spin coated at 1000 rpm for 10 s and then at 3000 rpm for 30 s; during the second step, 230 μL of chlorobenzene was dropped on top of the surface. For nanocrystal-based cells, first SiO$_2$ nanoparticles were deposited by dip coating as previously mentioned and then a perovskite precursor solution was infiltrated by spin coating. In this case an MAI and PbCl$_2$ mixture (3:1 molar ratio) in DMF was used, deposited at 5000 rpm for 60 s. The HTL was deposited by dripping a 70 mM Spiro-OMeTAD solution in chlorobenzene on top of the substrate, by spin coating at 4000 rpm for 30 s. FK209 (tris(2-(1 H-pyrazol-1-yl)-4-tert-butylpyridine)-cobalt(III)tris(bis (trifluoro-methylsulfonyl) imide)), LiTFSI (lithium bis (trifluoromethylsulphonyl)imide) and t-BP (4-tert-butylpyridine) were used as additives with 0.03, 0.5, and 3.30 molar ratio, respectively. Following this, 70 nm of gold was used as cathode, which was thermally evaporated atop the HTL under a vacuum level between 10^{-5} and 10^{-6} Torr.

Solar Cell Characterization: J–V characterization was performed with a digital sourcemeter (Keithley 2400) coupled solar simulator (Sun 2000, Abet Technologies) including a 150 W arc xenon lamp and the appropriate filter to replicate the AM1.5 solar spectra at 1 sun (confirmed by certificated silicon solar cell). A black mask with an aperture area of 0.125 cm^2 was used. IPCE was measured by a home-built system composed of a 300 W xenon lamp, a monochromator with 1140 g mm^{-1} grating (Model 272, McPherson) controlled by a digital scan drive system (Model 789A-3, McPherson), and a picoammeter (Keithley 6485). The response was corrected using a calibrated silicon photodiode (D8-Si-100 TO-8 Detector, Sphere Optics).

Impedance spectroscopy was performed using an Autolab PGSTAT204 (Metrohm) with an integrated FRA32M module. Spectra analysis and equivalents circuits were done with NOVA software (Metrohm). Data were obtained from 1 MHz to 0.01 Hz, measuring ten frequencies by decade with a sinusoidal perturbation of 0.02 V.

Supporting Information

Supporting Information is available from the Wiley Online Library or from the author.

Conflict of Interest

The authors declare no conflict of interest.

Data Availability Statement

Research data are not shared.

Keywords

[1] Editorial, *Nat. Energy* **2020**, *5*, 1.

[2] A. Kojima, K. Teshima, Y. Shirai, T. Miyasaka, *J. Am. Chem. Soc.* **2009**, *131*, 6050.

[3] https://www.nrel.gov/pv/assets/pdfs/cell-pv-eff-emergingpv.202001042.pdf (accessed: March 2021).

[4] D. H. Kang, N. G. Park, *Adv. Mater.* **2019**, *31*, 1805214.

[5] W. Rehman, D. P. McMeekin, J. B. Patel, R. L. Milot, M. B. Johnston, H. J. Snaith, L. M. Herz, *Energy Environ. Sci.* **2017**, *10*, 361.

[6] L. Meng, J. You, Y. Yang, *Nat. Commun.* **2018**, *9*, 5265.

[7] L. C. Schmidt, A. Pertegás, S. González-Carrero, O. Malinkiewicz, S. Agouram, G. Mínguez Espallargas, H. J. Bolink, R. E. Galian, J. Pérez-Prieto, *J. Am. Chem. Soc.* **2014**, *136*, 850.

[8] H. Lee, H.-J. Song, M. Shim, C. Lee, *Energy Environ. Sci.* **2020**, *13*, 404.

[9] H. Lu, Z. Huang, M. S. Martinez, J. C. Johnson, J. M. Luther, *Energy Environ. Sci.* **2020**, *13*, 1347.

[10] K. Lin, J. Xing, L. N. Quan, F. Pelayo García de Arquer, X. Gong, J. Lu, L. Xie, W. Zhao, D. Zhang, C. Yan, W. Li, X. Liu, Y. Lu, J. Kirman, E. H. Sargent, Q. Xiong, Z. Wei, *Nature* **2018**, *562*, 245.

[11] W. Zheng, P. Huang, Z. Gong, D. Tu, J. Xu, Q. Zou, R. Li, W. You, J. G. Bünzli, X. Chen, *Nat. Commun.* **2018**, *9*, 3462.

[12] M. Li, R. Begum, J. Fu, Q. Xu, T. Ming Koh, S. A. Veldhuis, M. Grätzel, N. Mathews, S. Mhaisalkar, T. Chien Sum, *Nat. Commun.* **2018**, *9*, 4197.

[13] Q. A. Akkerman, G. Rainò, M. V. Kovalenko, L. Manna, *Nat. Mater.* **2018**, *17*, 394.

[14] L. Fu, H. Li, L. Wang, R. Yin, B. Li, L. Yin, *Energy Environ. Sci.* **2020**, *13*, 4017.

[15] Y. Wei, Z. Cheng, J. Lin, *Chem. Soc. Rev.* **2019**, *48*, 310.

[16] M. Anaya, G. Lozano, M. E. Calvo, H. Míguez, *Joule* **2017**, *1*, 769.

[17] J. H. Im, C. R. Lee, J. W. Lee, S. W. Park, N. G. Park, *Nanoscale* **2011**, *3*, 4088.

[18] S. M. Yoo, S. J. Yoon, J. A. Anta, H. J. Lee, P. P. Boix, I. Mora-Seró, *Joule* **2019**, *3*, 2535.

[19] H. J. Lee, K. T. Cho, S. Paek, Y. Lee, A. J. Huckaba, V. I. E. Queloz, I. Zimmermann, G. Grancini, E. Oveisi, S. M. Yoo, S. Y. Lee, T. Shin, M. Kim, M. K. Nazeeruddin, *Adv. Funct. Mater.* **2018**, *28*, 1803801.

[20] S. M. Yoo, S. Y. Lee, E. Velilla Hernandez, M. Kim, G. Kim, T. Shin, M. K. Nazeeruddin, I. Mora-Seró, H. J. Lee, *ChemSusChem.* **2020**, *13*, 2571.

[21] H. C. Kwon, A. Kim, H. Lee, D. Lee, S. Jeong, J. Moon, *Adv. Energy Mater.* **2016**, *6*, 1601055.

[22] D. Bi, S. J. Moon, L. Häggman, G. Boschloo, L. Yang, E. M. J. Johansson, M. K. Nazeeruddin, M. Grätzel, A. Hagfeldt, *RSC Adv.* **2013**, *3*, 18762.

[23] S. H. Hwang, J. Roh, J. Lee, J. Ryu, J. Yun, J. Jang, *J. Mater. Chem. A* **2014**, *2*, 16429.

[24] N. Li, H. Li, Y. Li, S. Wang, L. Wang, *Phys. Chem. Chem. Phys.* **2015**, *17*, 24092.

[25] K. Lee, C. M. Yoon, J. Noh, J. Jang, *Chem. Commun.* **2016**, *52*, 4231.

[26] X. Yu, S. Chen, K. Yan, X. Cai, H. Hu, M. Peng, B. Chen, B. Dong, X. Gao, D. Zou, *J. Power Sources* **2016**, *325*, 534.

[27] L. Protesescu, S. Yakunin, M. I. Bodnarchuk, F. Krieg, R. Caputo, C. H. Hendon, R. Xi Yang, A. Walsh, M. V. Kovalenko, *Nano Lett.* **2015**, *15*, 3692.

[28] A. Swarnkar, A. R. Marshall, E. M. Sanehira, B. D. Chernomordik, D. T. Moore, J. A. Christians, T. Chakrabarti, J. M. Luther, *Science* **2016**, *354*, 92.

[29] M. Hao, Y. Bai, S. Zeiske, L. Ren, J. Liu, Y. Yuan, N. Zarrabi, N. Cheng, M. Ghasemi, P. Chen, M. Lyu, D. He, J. Yun, Y. Du, Y. Wang, S. Ding, A. Armin, P. Meredith, G. Liu, H. Cheng, L. Wang, *Nat. Energy* **2020**, *5*, 79.

[30] J. Yuan, A. Hazarika, Q. Zhao, X. Ling, T. Moot, W. Ma, J. M. Luther, *Joule* **2020**, *4*, 1160.

[31] M. Que, L. Zhu, Y. Guo, W. Que, S. Yun, *J. Mater. Chem. C* **2020**, *8*, 5321.

[32] F. Zhou, Z. Li, H. Chen, Q. Wang, L. Ding, Z. Jin, *Nano Energy* **2020**, *73*, 104757.

[33] A. Wang, Z. Jin, M. Cheng, F. Hao, L. Ding, *J. Energy Chem.* **2021**, *52*, 351.

[34] K. Chen, Q. Zhong, W. Chen, B. Sang, Y. Wang, T. Yang, Y. Liu, Y. Zhang, H. Zhang, *Adv. Funct. Mater.* **2019**, *29*, 1900991.

[35] Q. Zhao, A. Hazarika, X. Chen, S. P. Harvey, B. W. Larson, G. R. Teeter, J. Liu, T. Song, C. Xiao, L. Shaw, M. Zhang, G. Li, M. C. Beard, J. M. Luther, *Nat. Commun.* **2019**, *10*, 2842.

[36] M. Anaya, A. Rubino, T. C. Rojas, J. F. Galisteo-López, M. E. Calvo, H. Míguez, *Adv. Opt. Mater.* **2017**, *5*, 3.

[37] A. Rubino, M. Anaya, J. F. Galisteo-López, T. C. Rojas, M. E. Calvo, H. Míguez, *ACS Appl. Mater. Interfaces* **2018**, *10*, 38334.

[38] V. Malgras, S. Tominaka, J. W. Ryan, J. Henzie, T. Takei, K. Ohara, Y. Yamauchi, *J. Am. Chem. Soc.* **2016**, *138*, 13874.

[39] D. N. Dirin, L. Protesescu, D. Trummer, I. V. Kochetygov, S. Yakunin, F. Krumeich, N. P. Stadie, M. V. Kovalenko, *Nano Lett.* **2016**, *9*, 5866.

[40] A. Rubino, L. Caliò, A. García-Bennett, M. E. Calvo, H. Míguez, *Adv. Opt. Mater.* **2020**, *8*, 1901868.

[41] K. Tanaka, T. Takahashi, T. Ban, T. Kondo, K. Uchida, N. Miura, *Solid State Commun.* **2003**, *127*, 619.

[42] L. Brus, *J. Phys. Chem.* **1986**, *90*, 2555.

[43] J. Bisquert, E. J. Juarez-Perez, *J. Phys. Chem. Lett.* **2019**, *10*, 5889.

[44] I. Zarazua, G. Han, P. P. Boix, S. Mhaisalkar, F. Fabregat-Santiago, I. Mora-Seró, J. Bisquert,, G. Garcia-Belmonte, *J. Phys. Chem. Lett.* **2016**, *7*, 5105.

[45] V. Gonzalez Pedro, E. J. Juarez-Perez, W. S. Arsyad, E. M. Barea, F. Fabregat-Santiago, I. Mora-Sero, J. Bisquert, *Nano Lett.* **2014**, *14*, 888.

[46] J. Bisquert, I. Mora-Sero, F. Fabregat-Santiago, *ChemElectroChem* **2014**, *1*, 289.

[47] A. Dualeh, T. Moehl, N. Tétreault, J. Teuscher, P. Gao, M. K. Nazeeruddin, M. Grätzel, *ACS Nano* **2014**, *8*, 362.